Electro-structural regulation of vapour-limited energy extraction in safety-critical quenching systems

Inbaoli A[a], Sujith Kumar C S[a,b,*], Sandesh S. Chougule[b,c], Christos N. Markides[b]

[a] *Department of Mechanical Engineering, National Institute of Technology Calicut, Kerala-673601, India*

[b] *Clean Energy Processes (CEP) Laboratory, Department of Chemical Engineering, Imperial College London, London SW7 2AZ, United Kingdom*

[c] *Laboratoire de Génie Civil et Génie Mécanique (LGCGM), Université de Rennes, Rennes 35000, France*

[*] *Corresponding author: sujithcs@nitc.ac.in*

NB: This is the ACCEPTED MANUSCRIPT version of this Article. The final, published version of the article can be found at: https://doi.org/10.1016/j.energy.2026.141308

Abstract

Managing extreme thermal loads in safety-critical quenching and emergency cooling systems remains a critical bottleneck for energy-intensive industrial processes, where vapour-mediated interfacial resistance suppresses energy extraction and constrains operational stability. Existing passive and active strategies are constrained by their inherent latency in enabling effective thermal energy transport pathways during critical transient cooling periods. To address this bottleneck, a hybrid strategy is developed that couples an additive manufactured point-contact cellular surface architecture with electrohydrodynamic (EHD) interfacial actuation. The synergistic effects of architected interfacial pathways and EHD actuation are evaluated on stainless steel (SS316L) substrates using high-speed visualization and transient heat flux analysis. The hybrid approach effectively suppresses vapour-mediated insulation, increasing the minimum film boiling temperature (T_{min}) from 281 °C to 436 °C. By expanding the operational window of efficient cooling to higher temperatures, the system achieves 2.7 times increase in cumulative energy extraction, reaching 1.8 MJ/m² during the critical initial period of quenching. Furthermore, the active control modulates the energy release profile, converting stochastic thermal shock into a rate-controlled dissipation trajectory. These results establish a scalable design principle for safety-critical systems, in which energy extraction rate, operational stability, and auxiliary energy cost are simultaneously constrained.

Keywords

additive manufacturing, boiling, electrohydrodynamic, process intensification, transient cooling

Nomenclature

Symbols

c_p	Specific heat capacity (J/kg.K)
D_{cell}	Characteristic cell dimension (m)
E	Electric field strength (V/m)
$E_{n,l}$	Normal electric field at liquid interface (V/m)
F	Faraday constant (C/mol)
g	Gravitational acceleration (m/s^2)
h_{eff}	Effective heat transfer coefficient (W/m^2.K)
h_r	Linearized radiation heat transfer coefficient (W/m^2.K)
k	Thermal conductivity (W/m.K)
k_B	Boltzmann constant (J/K)
m	Global time steps (s)
N_A	Avogadro constant (1/mol)
P_{es}	Maxwell electrostatic stress (Pa)
q	Boundary heat flux (W/m²)
R	Gas constant (J/mol.K)
R''_{th}	Interfacial thermal resistance (m^2.K/W)
r	Sample radius (m)
$\dot{S}''_{gen}$	Entropy generation rate per unit area (W/m²·K)
T_{ini}	Initial temperature (°C, K)
T_{min}	Minimum film boiling temperature (°C, K)
T_{sat}	Saturation temperature (°C, K)
T_w	Wall temperature (°C, K)
$\dot{X}''_{dest}$	Exergy destruction rate per unit area (W/m²)
Y_j	Measured temperature at j^{th} sensor (°C, K)
Δq	Correction term
ΔT_s	Wall superheat (°C, K)

Greek

ϵ_0	Permittivity of vacuum (F/m)
ϵ_l	Permittivity of liquid phase (F/m)
ϵ_v	Permittivity of vapour phase (F/m)
δ	Vapour film thickness (m)
κ^{-1}	Debye length (m)
λ_H	Instability wavelength (m)
ρ	Density (kg/m^3)
σ	Surface tension (N/m)
Φ	Electric potential (V)
$\emptyset$	Sensitivity coefficient (K.m^2/W)
μ_{ion}	Ionic mobility (m²/V·s)
v	Drift velocity (m/s)

Subscripts

0	Reference or ambient condition
c	Computed value
cell	Cellular structure
dest	Destruction
eff	Effective
es	Electrostatic stress
gen	Generation
H	Hydrodynamic instability
ini	Initial
ion	ionic species
j	Sensor
l	Liquid phase
min	Minimum
v	Vapour phase
s	Superheat
sat	Saturation condition
w	Wall

1. Introduction

Managing extreme thermal loads fundamentally constrains the energy efficiency of heavy industrial processing and high-power electronic infrastructure. In sectors ranging from advanced metallurgy to power generation, thermal energy extraction rates directly dictate production throughput and operational safety [1]. Inefficient heat removal strategies prolong cycle times and increase specific energy consumption, constituting a substantial source of industrial energy waste [2]. As system power densities escalate, rapid and controlled energy extraction determines system viability [3] and economic performance [4]. A thermal resistance barrier forms spontaneously during peak load operations, limiting performance in high-flux environments. The barrier insulates the component and severs the thermal connection between the heat source and the coolant [5]. Consequently, energy extraction rates decline, causing uncontrolled temperature excursions that compromise material integrity and system reliability.

The operational constraint intensifies during transient operational phases, such as rapid quenching cycles or emergency power-down events. Conventional thermal management systems are inherently constrained by their latency in restoring effective cooling pathways rapidly enough to accommodate changing thermal loads under dynamic conditions [6]. Because current systems cannot actively modulate heat extraction rates during critical windows, operators rely on conservative, energy-intensive safety margins. Further, existing thermal management strategies aimed at restoring high-rate energy extraction under vapour-dominated transient conditions often incur prohibitive auxiliary energy costs or sacrifice operational stability. Therefore, next-generation energy systems require strategies that actively breach the thermal barrier and accelerate thermal energy transfer restoration to minimize energy waste and ensure stability [7].

The operational bottleneck arises physically from the Leidenfrost phenomena. The Leidenfrost state creates an operational bottleneck by forming a stable, insulating vapour layer at the solid–liquid interface [8]. Rapid vapour generation sustains a continuous vapour blanket that separates the coolant from the high-temperature surface. The vapour barrier increases thermal resistance and stalls energy extraction. Conventional passive approaches manage these interfacial dynamics by modifying coolant thermophysical properties [9] or engineering the boiling surface [10]. For instance, depositing porous layers via alumina nanofluids improves capillary-driven flow and nucleation activity [11]. However, these additive-based methods introduce operational liabilities. Excessive nanoparticle deposition creates transport resistance, while dissolved salts pose erosion and spalling hazards that compromise structural integrity and infrastructure lifespan. Alternative strategies involving stochastic porous materials, such as

foams [12], address surface area constraints but introduce substantial hydraulic bottlenecks [13]. The disordered, tortuous pore structure of these materials frequently traps gas, impeding release and creating localized instabilities. To resolve these geometric limitations, Kou et al. [14] demonstrated that ordered, periodic lattice structures fabricated via 3-D printing suppress bubble coalescence and entrapment. By replacing random pore networks with deterministic flow paths, these engineered architectures ensure rapid phase separation. Collectively, these findings establish that ordered, predictable geometries outperform stochastic structures for maintaining system stability under high-load conditions [15].

Despite the stability improvements provided by ordered geometries, passive strategies for managing vapour-mediated interfacial resistance remain constrained under the high-flux [16], transient conditions relevant to practical thermal processing and safety-critical cooling operations. Passive architectures, including additively manufactured or wettability modulated surfaces [17], rely on a static balance of buoyancy, capillary, and drag forces to guide vapour removal. Transient thermal loading overwhelms this balance, causing intense bubble coalescence and forming a persistent insulating vapour layer that restricts energy extraction rates and compromises operational stability [18,19].

On the other hand, active strategies mitigate the insulating vapour phase by inducing bulk fluid motion via forced convection [20] or jet impingement [21]. Alternative method involves applying discrete energy fields to manipulate the liquid-vapour interface [22]. Although bulk liquid circulation increases cooling capacity [23], hydraulic instabilities [24,25] and non-uniform pressure gradients [26] compromise performance. Furthermore, mechanical pumps introduce an additional energy load. The resulting energy penalty degrades net system efficiency. Active methods therefore compel a trade-off between enhanced heat transfer and operational cost.

Field-based techniques restrict actuation to the phase interface to mitigate the additional energy costs inherent to bulk fluid displacement. By modulating forces directly at the liquid-vapour boundary rather than accelerating the total fluid volume, such interventions minimize the energy expenditure required to disrupt the thermal barrier. However, magnetic or centrifugal systems often require cumbersome infrastructure, including heavy permanent magnets [27] or rotating assemblies [28]. These hardware dependencies create integration bottlenecks and limit scalability in compact energy systems. Electrohydrodynamic (EHD) forces offer a geometrically flexible alternative. Celestini et al. [29] demonstrated that applying a DC electric field suppresses the insulating vapour layer (Leidenfrost state) by inducing electrostatic attraction. By utilizing EHD stresses to destabilize the vapour film, this electrokinetic strategy

overcomes the thermal limitations of passive boiling without incurring the hydraulic energy penalties associated with mechanical pumping. Consequently, substituting bulk actuation with interface-targeted EHD stresses optimizes net system energy efficiency. However, when applied to smooth, unstructured surfaces, these methods encounter saturation effects such as contact angle saturation [30] and vapour elongation [31] that promote vapour accumulation rather than eliminating it. These limitations indicate that neither passive structuring nor active forcing alone ensures stable energy dissipation under transient, vapour-dominated conditions

Recent efforts combining structural modification with active energy field attempt to resolve the operational limitations of isolated strategies. For example, Wei et al. [32] experimentally demonstrated that attaching a passive honeycomb plate to the electrode promoted the directional phase separation. However, their work used the non-conductive porous ceramic structure ($CaO.Al_2O_3$ fused SiO_2 and TiO_2) as an attachment which introduces an additional high-resistance pathway and non-uniform field distribution. These drawbacks limit broader applicability and obscure the role of conductive, architected surface integration in sustaining reliable high-rate energy extraction. Therefore, existing studies provide limited guidance on deploying electrically conductive ordered porous geometries to alleviate vapour-mediated transport resistance during transient operation.

A critical assessment of the literature reveals two unresolved gaps relevant to energy systems regarding the architectural integration and dynamic regulation of these vapour-management strategies. First, most structured surface strategies rely on full-contact integration via direct fabrication or bonded porous layers, for maximizing surface contact and enhancing energy transport. Alternative architectural concepts that exploit partial or point-contact integration to enforce localized pressure gradients and directional vapour expulsion remain largely unexplored. Second, majority of passive and active enhancement studies evaluate performance under steady-state conditions, even though many industrial thermal processes and emergency cooling scenarios are inherently transient. As a result, there is a need for experimentally validated strategies capable of sustaining high and predictable energy extraction rates during the critical initial stages of safety-critical quenching systems, when vapour insulation is most prevalent and operational risk is highest. Figure 1 schematically summarizes this limitation and the associated process-design challenge. The left panel shows the conventional operating regime, in which vapour-film formation introduces a high thermodynamic resistance that constrains the usable operating range and suppresses energy extraction under increasing thermal load. These limitations raise a fundamental process-design question: can active

interfacial actuation combine with architectural enforcement accelerate transient energy dissipation without affecting stability or introducing prohibitive auxiliary energy costs?

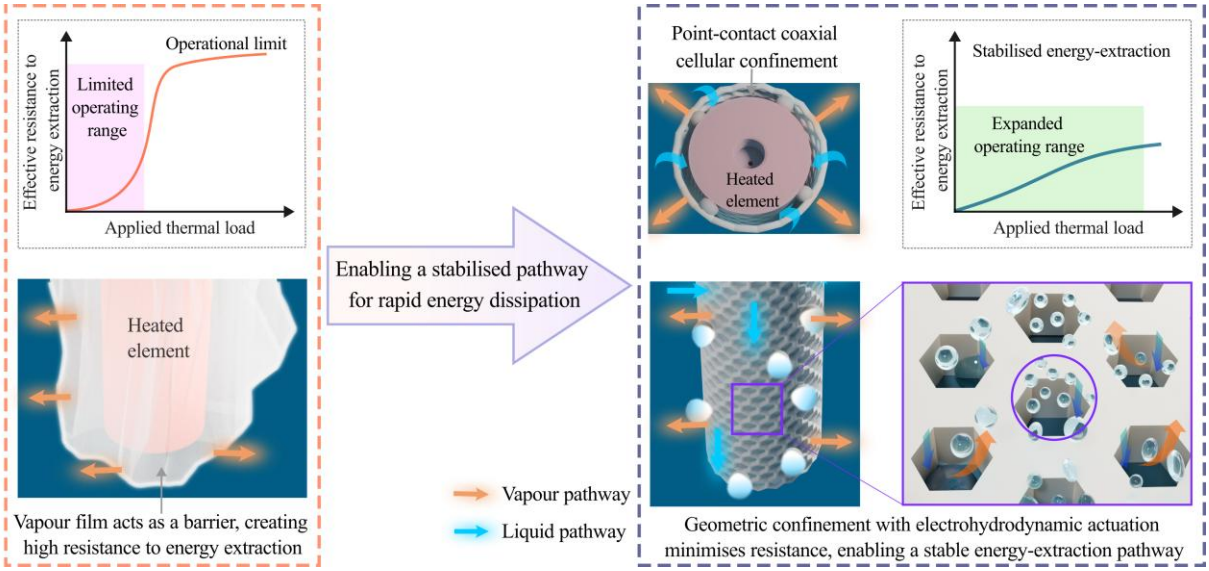


Figure 1. Process-design challenge and hybrid intensification framework: conventional vapour-mediated operational bottleneck (left panel). Active regulation via synergistic electro-architected control enabling high-rate energy extraction pathways (right panel).

To address this process-design challenge, a hybrid strategy is introduced that couples a conductive, point-contact surface architecture (cellular structure) with externally applied electric field. The strategy targets the stabilization and acceleration of transient energy dissipation at superheated surfaces, directly addressing reliability and throughput constraints inherent to vapour-limited thermal processes. Confined, pressurized regions formed through point-contact integration impose deterministic vapour expulsion and promote sustained liquid replenishment at the interface. In parallel, the applied electric field provides complementary interfacial actuation that destabilizes the insulating vapour layer during high-superheat operation. The combined architected interfacial pathways and EHD actuation enables faster and more predictable energy extraction during quenching, thereby extending the viable operating envelope of vapour-dominated thermal processes, as shown in Fig. 1 (right panel). The resulting framework provides practical design principle for active two-phase systems in which operational stability, processing throughput, and energy efficiency are simultaneously constrained. Emphasis is placed on sustaining reliable high-rate energy dissipation during the most critical phases of thermal operation, aligning the proposed approach with the performance and reliability requirements of high-energy-intensive systems.

2. Experimental methods

In this work, a transient immersion cooling platform was employed to investigate the active regulation of vapour-mediated thermal resistance under transient high-flux conditions. The experimental framework is specifically designed to replicate the adverse thermal constraints characteristic of safety-critical quenching systems and emergency core cooling systems, where the formation of a stable, insulating vapour layer imposes a fundamental limit on energy extraction rates and system reliability [33]. The following sections detail the experimental apparatus, operational procedure, data reduction, and uncertainty analysis.

2.1 Experimental apparatus

Figure 2(a) schematically depicts the experimental test facility. The facility comprises a customized ceramic tubular furnace, a programmable electronic slider, an electrolyte bath, test section, a data acquisition system (National Instruments NI9212), high-speed camera (PHANTOM MIRO LAB110), and a DC power supply.

The tubular furnace capable of reaching 900 °C, under the control of an integrated proportional-integral-derivative (PID) controller and K-type thermocouples was employed to heat the sample. The sample was suspended from the tail end of a stainless-steel holder, with the front end affixed to an electronic slider. A programmable single-axis vertical slider equipped with limit switches was used to immerse the heated sample into the bath with minimal motion perturbations. To minimize radiation heat losses, the sample was rapidly submerged into the electrolyte bath at a velocity of 200 mm/s. The electrolyte bath is the 2.5 L transparent borosilicate container. The transparent configuration allowed for high-resolution visualization of interfacial phenomena, including bubble layer formation and vapour coalescence on the test sample.

The test section and electrolyte solution preparation were detailed in Section 2.2. The temperature of the sample was acquired via a 1 mm diameter K-type thermocouple (uncertainty ± 4 °C at 800 °C), embedded within the sample using high-temperature thermal conductive paste. Further, temperature of the electrolyte was monitored at three distinct locations within the bath using K-type thermocouples. The thermocouples were interfaced with LabView via a NI9212 data acquisition unit. Bubble dynamics and vapour layer behaviour were captured using a PHANTOM MIRO LAB110 high-speed camera with a maximum resolution of 1280 × 800 pixels at 3000 frames/s. Additional details regarding the experimental arrangement can be found in Refs. [34,35]. An external DC power source (maximum output: 1000 V, 1 A) was used to apply an electric potential across the sample during the experiments.

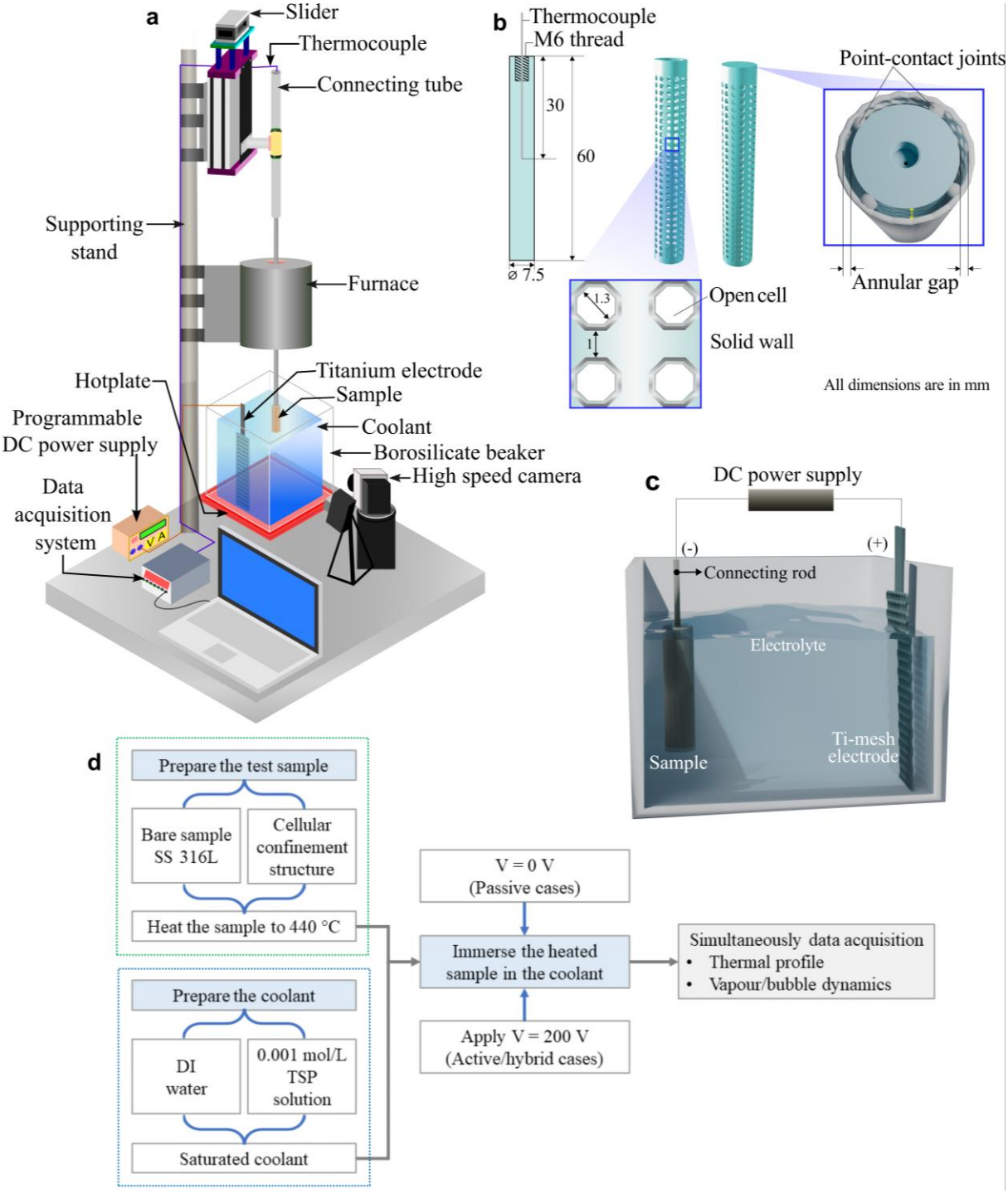


Figure 2. Experimental test facility: (a) schematic diagram of the test apparatus; (b) sample details: bare sample, additively manufactured cellular structure, and point-contact coaxial cellular confinement structure (magnified image shows the discrete contact points and annular gap between the bare sample and cellular structure); (c) hybrid quenching system with sample as cathode and Ti electrode as an anode; and (d) operational procedure.

The voltage and current were monitored using a VI acquisition system with a sampling frequency of 100 Hz. Here, an optimized voltage of 200 V was selected based on the prior

detailed investigation [36]. In this configuration, the sample was connected to the cathode terminal, while a counter electrode Titanium Grade 1 ASTM B265 as a 0.9 mm thick w-type mesh (dimensions: 150 mm × 50 mm) was connected to the anode terminal.

2.2 Test sample and coolant preparation

The SS316L alloy was selected as the sample material due to its excellent corrosion resistance at high-temperature aqueous environment and ease of micromachining [37] for embedding the thermocouples. The SS316L rod was machined to the desired dimensions of 7.50 ± 0.14 mm in diameter and 60 ± 0.1 mm in length (see Fig. 2(b) for sample details). This high aspect ratio design ensures that heat dissipation predominantly occurs in the radial direction during immersion quenching [38–40]. Following the machining, internal threading was performed at one end of the rod to facilitate attachment to the holder. At the threaded end, a blind hole of 1 mm in diameter was drilled to the rod's centre, as depicted in Fig. 2(b), for the fixation of a thermocouple. The samples were subsequently polished using emery papers ranging from #400 to #2000, followed by a 10 min ultra-sonication in acetone and another 10 min cycle in DI water. Finally, the specimens were dried in an oven at 100 °C for 2 h to eliminate any residual moisture.

To develop an enhanced electrode architecture, an additively manufactured three-dimensional interconnected cellular structure was prepared using the laser powder bed fusion technique. The SS316L cellular structure, with a length of 61 ± 0.2 mm and outer diameter of 10 ± 0.1 mm, was fabricated using a selective laser melting (SLM) machine equipped with a Yb-fibre laser. The fabrication parameters were as follows: laser power of 275 W, layer thickness of 0.05 mm, hatching distance of 0.12 mm, scan speed of 700 mm/s, and an energy density of 66 J/mm³. The cell width and wall thickness of the structure, shown in Fig. 2(b), were designed such that the cell width was smaller than the bubble diameter observed on the bare sample. Figure 2(b) presents the computer-aided design (CAD) models of the standalone 3-D cellular structure and the integrated sample. The additive manufactured cellular structure was welded to the SS316L cylindrical rod using micro plasma welding (Make and model: ARCRAFT and MP25F). Here, the welding process involves discrete spot weld instead of continuous stream of weld. The resulting point-contact arrangement provides the intended coaxial geometry, maintaining the annular gap (Fig. 2b). Finally, the integrated sample (cellular structure + bare sample) was ultrasonicated in acetone and DI water, and dried in an oven for 2 h. The obtained specimen is herein designated as the point-contact coaxial cellular confinement structure.

An ionic additive, trisodium phosphate (TSP), was employed for its demonstrated capability to enhance heat dissipation during quenching [35]. Consistent with the investigations of Kumar et al. [41], a minimal concentration of 0.001 mol/L TSP was utilized to achieve the desired heat transfer enhancement without surface fouling or significant altercation of the thermal properties of the coolant. The preparation involved dissolving TSP (Sigma Aldrich; purity ~96%) in DI water (Merck, Milli-Q) to yield a 0.001 mol/L solution, followed by stirring on a magnetic stirrer for 45 min. This low concentration minimizes froth formation during boiling, reduces surface deposition, and preserves the thermophysical properties of the fluid. Notably, the cooling solutions were prepared 6–8 h in advance to ensure complete dissolution DI water.

2.3 Experimental procedure

The immersion cooling experiments were performed using both the bare sample and the sample with cellular structure under conditions with and without a DC electric field, in DI water and a 0.001 mol/L TSP solution. The electrochemical system with sample as cathode and Ti electrode as an anode is shown in Fig. 2(c). Figure 2 (d) shows a flowchart outlining the experimental procedures for the passive, active, and hybrid cooling approaches. Initially, DI water was subjected to vigorous nucleate boiling to facilitate degassing, and the resultant degassed DI water was used as the base coolant for all tests. The coolant bath was filled with 2 L of degassed DI water and heated to the saturation temperature. Concurrently, the sample was heated within the furnace to 440 °C and maintained at that temperature for 45 min, with both sample and bath temperatures continuously monitored via the data acquisition system.

Upon reaching the target temperature and soaking time, the sample was immersed into the saturated DI water using the electronic slider. During cooling, the temperature profile was recorded via LabView, while vapour layer and bubble dynamics were captured by the high-speed camera. Data logging continued until thermal equilibrium between the sample and the coolant was established, thereby concluding the experiment. In experiments involving electric field-assisted immersion cooling, the DC electric field was applied between the sample and the counter electrode. Each experimental condition was repeated for a minimum of five test runs using fresh samples, with the average values used for subsequent data processing.

2.4 Data reduction

The unknown boundary heat flux at the sample surface was computed using the knowledge of temperature data at selected interior point of the sample via serial inverse heat conduction algorithm proposed in Refs. [42–44]. A finite element domain was modelled, and inverse heat

conduction algorithm was solved using TmmFE (Thermal-mechanical-metallurgical Finite Elements) Inverse Solver Ver. 45. The following section details the finite element model and governing equations for computing the heat flux.

2.4.1 Finite element model

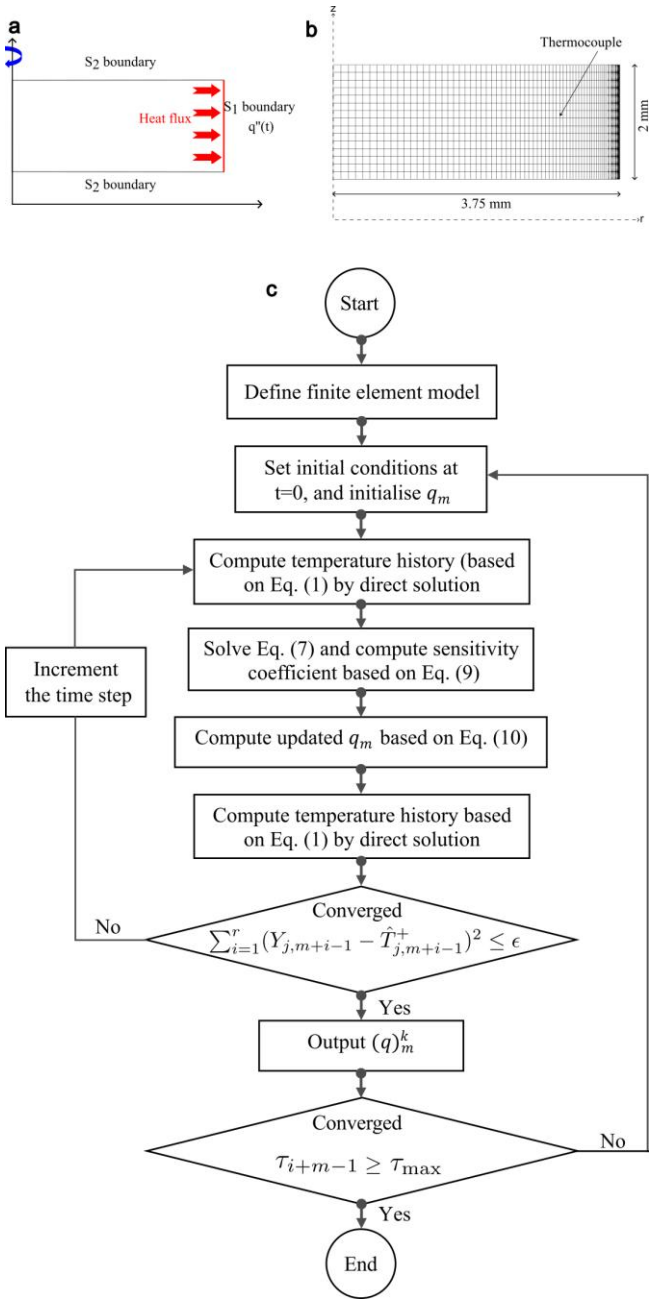
A single unknown heat flux at the boundary was assumed along the sample surface. Figure 3(a) shows the computational domain and the boundary conditions. The computational domain is a 2-D axisymmetric representation of the solid SS316L cylinder, formulated in cylindrical coordinates (r, z). The domain represents the mid-section of the sample where the thermocouple was mounted. A similar model was also employed in the literature [45] to determine the boundary heat flux during the immersion cooling process. The grid of solution domain is shown in Fig. 3(b). The domain is discretised with 4-node quadrilateral finite elements arranged in a structured mesh generated using a 4-side linear patch with 1-side graded distribution. The grading concentrates elements towards the heat-flux boundary S_1, where spatial resolution is most critical for the accuracy. Each node carries a single temperature degree of freedom, consistent with the thermal-only formulation of the model. Following the mesh convergence study, the simulations were conducted using a total of 1250 grid elements (1326 nodes). Details of mesh convergence study are provided in the supplementary material. Boundary S_1 represents the unknown heat flux, the heat transfer at S_2 is negligible considering the length of the sample. Adiabatic condition is assumed along central axis of symmetry. Table 1 presents the boundary conditions use in the inverse heat conduction model for computing the heat flux at the surface.

2.4.2 Governing equations

Transient heat conduction within a 2-D computational domain in the cylindrical coordinate system is governed by [42,43]:

$$\frac{k}{r}\frac{\partial}{\partial \mathrm{r}}\left(r\frac{\partial T(r,z,t)}{\partial \mathrm{r}}\right)+k\frac{\partial}{\partial \mathrm{z}}\left(\frac{\partial T(r,z,t)}{\partial \mathrm{z}}\right)=\rho c_p\frac{\partial T(r,z,t)}{\partial t} \quad (1)$$

where $k, \rho,$ and c_p are the thermal conductivity, density and specific heat capacity of SS316L cylindrical sample. The thermophysical properties of SS316L were implemented in the inverse heat-conduction model as temperature-dependent functions. A detailed discussion is provided in the supplementary material.



283

284 **Figure 3.** (a) Computational domain; (b) grid of solution domain; and (c) inverse heat
285 conduction algorithm for heat flux determination.

286 **Table 1.** Boundary conditions for inverse heat transfer model.

Boundary surface	Boundary condition
S_1	$q(t) = -k\left(\frac{\partial T}{\partial r}\right), T_{(r,z,t)} = T(t)$
S_2	$q(t) = -k\left(\frac{\partial T}{\partial z}\right) = 0$

287 To solve the serial inverse heat conduction model for heat flux during immersion cooling the
288 initial and boundary conditions are defined below.

289 Initial condition:

$$T_{(r,z,t)} = T_{ini} \tag{2}$$

290 at $t = 0$ where $T_{ini} = T_c(t)$.

291 Boundary conditions:

$$-k\left(\frac{\partial T}{\partial r}\right) = q(t) \text{ on } S_1 \tag{3}$$

$$-k\left(\frac{\partial T}{\partial z}\right) = 0 \text{ on } S_2 \tag{4}$$

$$T_{(r,z,t)} = T(t) \text{ at } r = r_0 \tag{5}$$

$$t = 0 < t \leq t_{end} \tag{6}$$

292 where T_{ini} is the initial temperature of the sample after its complete immersion into the coolant,
293 $q(t)$ the unknown heat flux quantity, $T(t)$ the time-dependent temperature data, r_0 the radius
294 of the sample, and t_{end} the time of completion of immersion cooling process. Based on these
295 conditions the unknow boundary heat flux at S_1 was estimated. Figure 3(c) shows the algorithm
296 for estimating boundary heat flux using inverse heat conduction analysis.

297 To deduce the unknown heat flux, the objective function with respect to q is given by:

$$J(q_m) = \sum_{i=1}^{r} \left(Y_{j,m+i-1} - \hat{T}^{+}_{j,m+i-1}\right)^2 \tag{7}$$

298 where $J(q_m)$ is the linear least square norm, which is the sum of squared error between the
299 measured and computed temperature at the measuring point inside the sample. This
300 optimization is performed to minimize the difference between the measured and computed
301 temperatures in future time steps. Here, $Y_{j,m+i-1}$ is the measured temperature, $\hat{T}^{+}_{j,m+i-1}$ is the
302 computed temperature, j is the number of temperature sensors in the sample (j = 1 in the current
303 investigation), m is global time steps, i is the current time step and r is the total number of
304 future time steps ($r = 4$, is considered in the present investigation).

305 For initialization of the numerical solver an arbitrary value for q_m is assumed and then heat
306 conduction equation is solved for r future time steps. The optimization of $J(q)$ for q_m yields
307 the correction term for deducing heat flux in $m + i$ time step:

$$(\Delta q)^n_m = \frac{\sum_{i=1}^{r}\left[Y_{m+i-1} - \hat{T}_{m+i-1}\right]\phi_i^{n-1}}{\sum_{i=1}^{r}\left(\phi_i^{n-1}\right)^2} \tag{8}$$

308 where n is number of iterations, and ϕ_i^{k-1} is the sensitivity coefficient:

$$\phi_i^{n-1} = \frac{T_{m+i}\left(q_m^{n-1}(1+\epsilon)\right) - T_{m+i}(q_m^{n-1})}{\epsilon q_m^{n-1}} \quad (9)$$

The sensitivity coefficient signifies the variation in computed temperature for a slight change (ϵ) in $(q)_m$. Then this correction term is added to the obtained heat flux:

$$q_m^n = (q)_m^{n-1} + \frac{\sum_{i=1}^{r}\left[Y_{m+i-1} - \hat{T}_{m+i-1}\right]\phi_i^{n-1}}{\sum_{i=1}^{r}\left(\phi_i^{n-1}\right)^2} \quad (10)$$

This iteration procedure continues until the error between the measured and computed temperature minimize to the satisfies criterion:

$$\sum_{i=1}^{r}\left(Y_{j,m+i-1} - \hat{T}_{j,m+i-1}^{+}\right)^2 \leq \epsilon \quad (11)$$

where $\epsilon = 10^{-6}$. Once this condition is satisfied the iteration is stopped for time step τ_i and go to next time step τ_{i+1}. Then the obtained final iterative heat flux value is considered as the initial known heat flux value for next time steps. The loop ends when time $t = t_{end}$.

To assess the irreversibility associated with vapour-mediated thermal resistance, an exergy-based analysis was performed using the temperature and heat flux. The analysis evaluates entropy generation associated with heat transfer across a finite temperature difference between the solid surface and the saturated coolant. While local thermal non-equilibrium exists near the interface during film boiling, the use of a constant saturation temperature provides a conservative and reproducible reference consistent with system-level energy assessment. The instantaneous entropy generation rate per unit area ($\dot{S}''_{\text{gen}}(t)$) associated with heat transfer is:

$$\dot{S}''_{\text{gen}}(t) = q''(t)\left(\frac{1}{T_{\text{fluid}}} - \frac{1}{T_s(t)}\right) \quad (12)$$

and the local exergy destruction rate per unit area:

$$\dot{X}''_{\text{dest}}(t) = T_0\left[\dot{S}''_{\text{gen}}(t)\right] \quad (13)$$

2.5 Uncertainty analysis

In the immersion quenching experiments, the various parameters measured are temperature, voltage, current, weight of the additives, sample length, and diameter. The accuracies of the measuring equipment are listed in the Table 2. Heat flux was computed using inverse heat conduction analysis, and the cooling rate was computed from the time derivative of the sample temperature ($T_{(r,t)}$) throughout the immersion cooling process [46,47]. The maximum uncertainty in the derived parameters heat flux and cooling rate are determined using the

uncertainty analysis method developed by Blackwell and Deck [48]. For, instance, the heat flux estimation includes individual uncertainties in the parameters used:

$$\delta q^c = \sqrt{\sum_{i=1}^{n} \left(\frac{\partial q^c}{\partial x_i}\,\delta x_i\right)^2} \tag{14}$$

$$= \sqrt{\left[\frac{\partial q^c}{\partial \Delta T^m}\,\delta \Delta T^m\right]^2 + \left(\frac{\partial q^c}{\partial k}\,\delta k\right)^2 + \left(\frac{\partial q^c}{\partial C_p}\,\delta C\right)^2} \tag{15}$$

where ΔT^m, k and $C = \rho c_p$ are the parameters used for computing the heat flux. Table 3 summarizes the maximum uncertainty in heat flux and cooling rate.

Table 2. Details of accuracy of the measuring equipment.

Instrument/Sensor	Range	Variable measured	Accuracy
Vernier calliper	0-150 mm	Length, diameter	± 0.02 mm
Voltmeter	0-500 V	Voltage	± 0.1 V
Ammeter	0-200 mA	Current	± 0.1 mA
Thermocouple	0-800 °C	Temperature	± 4 °C [@ 800 °C]
Weighing machine	0-250 g	Mass	± 0.01 g
Measuring jar	0-500 mL	Volume	± 2 mL

Table 3. Summary of uncertainties in derived parameters.

Parameter	Uncertainty (max)
Heat flux	13%
Cooling rate	7%

3. Results and discussion

The experimental evaluation is structured to quantify the transition from vapour-limited instability to actively regulated thermal energy transport. The analysis first defines the baseline transport limitations by characterizing the high-impedance vapour barrier that constitutes the primary bottleneck during transient quenching. Subsequently, the hybrid strategy is assessed against this constraint using performance metrics, specifically the T_{min} and transient heat flux, to map the expansion of the safe operating envelope. Finally, these engineering metrics are synchronized with high-speed interfacial visualization to validate the physical mechanisms responsible for process intensification and restoring process control.

3.1 Quantification of baseline thermal latency and thermal energy transport constraints

The immersion cooling experiment using the unmodified SS316L sample establishes the baseline transport limitations of the passive quenching system. Upon initiation at 440 °C, the system enters a critical operational bottleneck characterized by the immediate formation of a stable vapour film (Fig. 4a). This vapour layer physically isolates the solid surface from the liquid coolant, creating a high-impedance thermal barrier that severely restricts energy dissipation. Consequently, the initial cooling phase is dominated by radiation and weak convective heat transfer across this insulating layer, resulting in a prolonged period of thermal lag. The total heat flux (q'') across the formed vapour film is:

$$q'' = q''_{cond} + q''_{rad} = \left(\frac{k_v}{\delta}\right)(T_w - T_{sat}) + h_r(T_w - T_{sat}) \quad (16)$$

where k_v is the thermal conductivity of the vapour (W/m·K), δ is the vapour film thickness (m), T_w and T_{sat} are the wall and saturation temperatures (K), and h_r is the linearized radiation heat transfer coefficient (W/m^2·K). As effective heat transfer coefficient (h_{eff}), is primarily limited by the conductive term $\left(\frac{k_v}{\delta} + h_r\right)$, the system performance is inversely proportional to the film thickness. The low thermal conductivity of the vapour creates a substantial interfacial thermal resistance $\left(R''_{th} = \frac{1}{h_{eff}}\right)$, which limits the average cooling rate to just 7.5 K/s. The observed rate represents a significant performance deficit compared to the peak cooling rate of 65 K/s achievable during the subsequent nucleate boiling regime (Fig. 4b).

High-speed visualization (Fig. 4b) confirms the hydrodynamic instability of this regime, revealing oscillatory behaviour at the liquid–vapour interface. The system remains in this high-thermal impedance state until the gradual thinning of the vapour layer culminates in its collapse, typically initiating at the bottom of the sample and progressing upward. This collapse, marked by the T_{min} of 281 °C, precipitates the transition to nucleate boiling, characterized by rapid bubble formation and surface rewetting. These observations align with established transient boiling behaviours reported in the literature [49,50]. However, in the context of safety-critical thermal management, the primary concern is the prevalence of the film boiling phase. The passive baseline system sustains this insulating regime for 23 s, imposing a critical thermal latency where the extraction of stored energy is severely hindered. This baseline characterization confirms that the stability of the vapour film is the governing constraint on system safety, defining the specific inertial delay that subsequent active control strategies must overcome to restore thermodynamic availability.

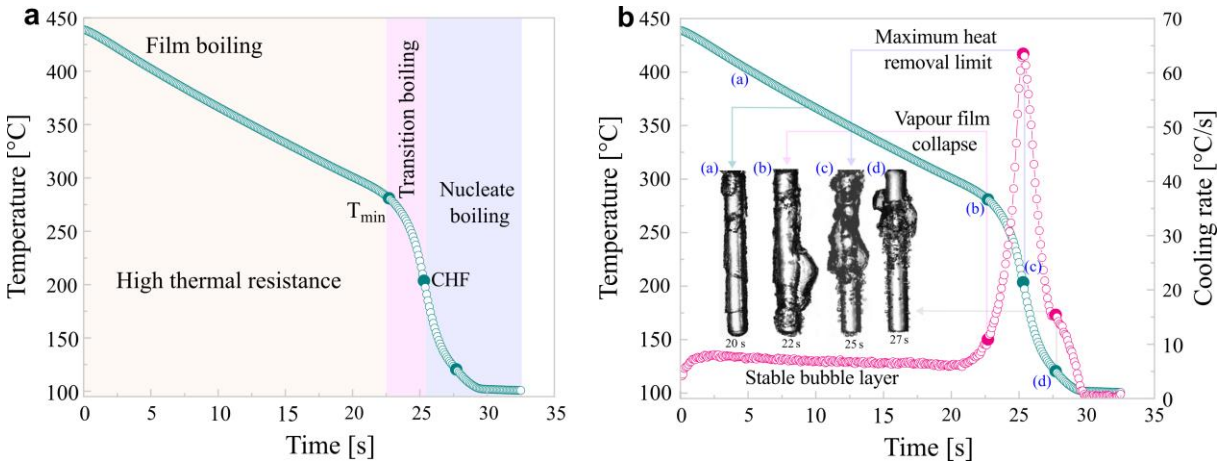


Figure 4. (a) Baseline performance characteristics of the system showing vapour-dominated thermal resistance; and (b) bubble dynamics and cooling rate characteristics of baseline system.

3.2 Process intensification via a hybrid strategy

The dominant transport limitation in high heat flux quenching systems is the masking of the heat transfer surface by stable vapour films, which imposes a severe interfacial thermal impedance and constrains safe energy dissipation. As established by Niblett et al. [51], the insulating vapour phase on the surface increases interfacial resistance and degrades transport efficiency. The developed hybrid strategy addresses this safety-critical bottleneck by enforcing deterministic vapour removal and continuous coolant access to the solid surface. By combining a cellular architecture with EHD actuation, the system maintains an expanded wetted area and suppresses vapour-dominated insulation across a wide operating envelope.

Figure 5(a) quantify the system-level impact of this hybrid thermal control strategy. The T_{min} increases from 281 °C to 436 °C, indicating that the system remains within transition and nucleate boiling regimes over a substantially wider temperature range. This shift reflects an expansion of the safe operating envelope rather than a peak-performance enhancement. Moreover, the hybrid configuration exhibits rate-controlled and temporally stable energy dissipation, in contrast to the uncontrolled thermal transients observed in the passive baseline. Figure 5(b) shows the instantaneous exergy destruction rate for both the baseline and hybrid configurations over the full quenching duration. Although both systems initiate from comparable thermal states, the temporal organization of irreversibility differs substantially.

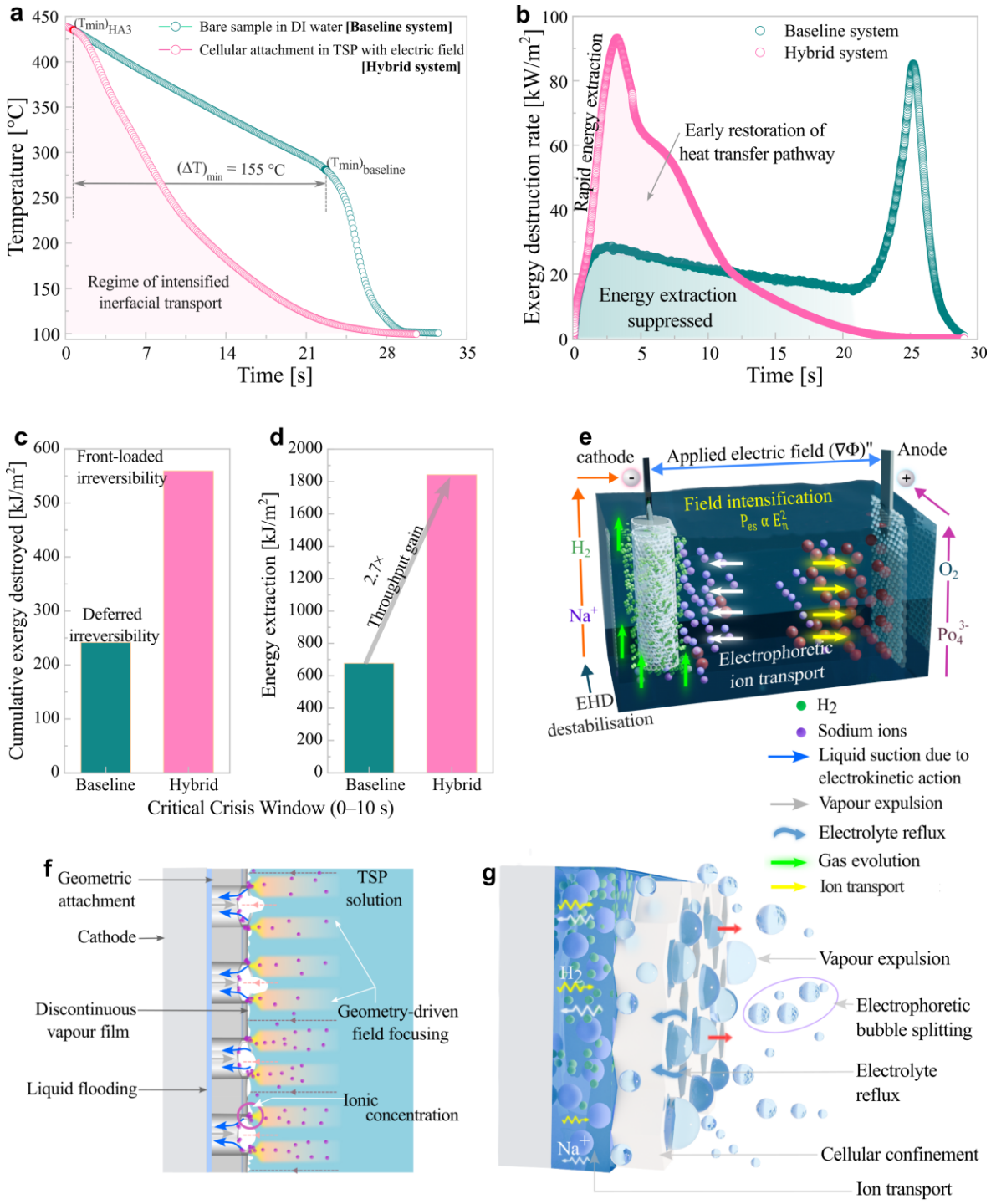


Figure 5. Process intensification: (a) performance of hybrid system in comparison to baseline system; (b) temporal evolution of exergy destruction in baseline and hybrid system; quantification of the critical process trade-off; (c, d) front-loading of irreversibility, and a cumulative energy extraction capacity (throughput) during the critical crisis window (0-10 s); (e) illustration of electrophoresis and bubble evolution in the hybrid system; (f) geometry-driven electric field concentration; and (g) enhanced EHD activity and bubble dynamics at the point-contact coaxial cellular confined structure.

In the hybrid configuration, the exergy destruction rate increases rapidly during the initial stage of quenching and reaches a global maximum at approximately $t \approx 3$ s, followed by a monotonic decay towards negligible values by $t \approx 25$ s (Fig. 5(b)). This temporal concentration indicates that the dominant irreversible processes are confined to the earliest phase of cooling, coinciding with the period of highest thermal gradients. The subsequent decay reflects the early restoration of effective thermal coupling between the solid and the coolant, thereby averting vapour-mediated insulation at high superheat conditions.

By contrast, the baseline system exhibits a markedly different evolution. After an initial rise, the exergy destruction rate remains at a quasi-steady plateau of approximately 25-30 kW/m² over an extended interval up to $t \approx 20$ s, followed by a delayed and pronounced global maximum near $t \approx 25$ s. This late-stage peak is indicative of sustained vapour-dominated thermal resistance, during which irreversibility accumulates and is released abruptly upon rewetting. In safety-critical quenching systems, such delayed irreversibility is undesirable, as it coincides with extended periods of poor controllability and elevated operational risk.

The two curves intersect at approximately $t \approx 12$ s, marking a transition in dominance. Prior to this point, the hybrid system exhibits a higher instantaneous exergy destruction rate, whereas beyond it the baseline system dominates. This crossover highlights a fundamental trade-off: the hybrid strategy concentrates irreversibility early in the quench in order to suppress prolonged and delayed exergy destruction later in the process. The cumulative exergy destruction, integrated over the first 10 s of quenching (Fig. 5(c)), provides a system-level measure of irreversibility during the most critical transient interval. Within this period, the hybrid system exhibits a cumulative exergy destruction of approximately 560 kJ/m², compared with 240 kJ/m² for the baseline configuration. Although the hybrid system therefore incurs greater total irreversibility during the early stage, this result must be interpreted in conjunction with the temporal distribution discussed above. In the hybrid case, irreversibility is localized within a short, controlled window, whereas in the baseline system it is deferred to later stages, where it coincides with unstable rewetting and abrupt thermal transitions. From an energy-systems perspective, irreversibility localization is preferable to irreversibility persistence. Concentrating entropy generation early in the quench reduces exposure time to vapour-dominated thermal resistance and limits the likelihood of delayed thermal excursions, which are particularly hazardous in safety-critical thermal operations.

Figure 5(d) compares the total energy extracted during the first 10 s of quenching, obtained by integrating the measured heat flux. Over this interval, the hybrid system extracts approximately

1.8 MJ/m². This corresponds to a 2.7-fold increase in energy extraction capacity and an absolute gain of 1.2 MJ/m². Importantly, this enhancement is achieved without extending the quenching duration, indicating a genuine increase in thermal throughput rather than a temporal redistribution of energy removal. When interpreted alongside the exergy results, this finding demonstrates that the hybrid configuration removes a substantially larger fraction of the stored thermal energy during the most thermodynamically consequential phase of the process. Although the hybrid system exhibits higher early exergy destruction, this penalty is offset by the significant increase in energy extracted prior to the onset of baseline rewetting instabilities. The combined energy and exergy analyses reveal a critical trade-off in transient quenching behaviour. The hybrid system accepts increased local irreversibility during the earliest stage of cooling in order to achieve a markedly higher energy extraction rate and to suppress delayed irreversibility associated with persistent vapour insulation.

In the baseline configuration, lower early exergy destruction does not correspond to improved performance; rather, it reflects ineffective heat transfer during the film boiling regime. The subsequent late-stage exergy peak coincides with abrupt thermal coupling of solid-coolant, which introduces risks of thermal shock. In contrast, the hybrid strategy front-loads irreversibility while maintaining continuous thermal contact, enabling smoother temperature decay and enhanced operational predictability. From a system-level energy perspective, this shift is advantageous. High-rate early energy extraction reduces residence time at extreme temperatures, while suppression of delayed irreversibility enhances stability and controllability. These results indicate that, in transient high-flux thermal processes, minimizing delayed or peak irreversibility is more critical than minimizing total early-stage irreversibility.

The physical mechanism underpinning this process control and intensification is shown schematically in Fig. 5(e-g). An externally applied electric field ($\nabla\Phi$), acts as a controllable actuator that modifies interfacial force balances at the liquid–vapour boundary. The architected conductive surface concentrates the electric field at geometric edges and corners, producing localized regions of elevated field intensity (Fig. 5(f)). These field gradients generate directed fluid motion and pressure asymmetries that promote vapour destabilization and liquid replenishment at the solid interface [52]. This developed charge structure modifies the local electric field distribution and interfacial dynamics.

The synergy between these effects plays a critical role in the intensification of interfacial transport. The resulting interfacial force amplification can be expressed through the Maxwell stress (P_{es}), which scales with the square of the normal electric field:

$$P_{es} = \frac{1}{2}\epsilon_l E_{n,l}^2 \left(\frac{\epsilon_l}{\epsilon_v} - 1\right) \quad (17)$$

where ϵ_l is the permittivity of liquid phase, ϵ_v represent the permittivity of vapour phase, and $E_{n,l}$ is the electric field components normal to the interface on the liquid domain. Geometric field focusing increases $E_{n,l}$ locally, thereby intensifying the destabilizing pressure acting on the vapour film. This pressure gradient accelerates vapour rupture and restores liquid–solid contact, enabling reliable heat extraction during high-superheat operation.

Once liquid-solid contact is re-established, the coupled action of geometric confinement and electrically induced interfacial forcing sustains a feedback loop of vapour expulsion and liquid replenishment. Vapour is preferentially channelled away from the surface, while liquid access is continuously restored, preventing re-formation of an insulating film. The resulting dispersed vapour structures suppress large-scale coalescence and stabilize interfacial transport, ensuring that the heat-transfer surface remains accessible throughout high-temperature operation. The observed enhancement in mass and energy transport performance is attributed to the synergistic interplay between the geometric confinement, the applied electric potential, and the consequent electrohydrodynamic activities at the surface. The enhanced energy transport observed here arises from the coordinated action of architectural confinement and active interfacial forcing. To establish robust design guidance for safety-critical thermal systems, the following sections deconstruct this hybrid approach by isolating the individual contributions of passive geometry, coolant modification, and active electrical actuation to the overall process intensification.

3.3 Mechanistic decoupling of passive confinement and active actuation effects

This section systematically decouples the hydrodynamic stabilization provided by passive architectural confinement from the active electrohydrodynamic actuation, quantifying the distinct roles of geometry and field forces in restoring thermodynamic accessibility.

3.3.1 Passive modifications of interfacial stability and hydrodynamics

Passive modifications to the coolant chemistry and surface geometry were evaluated to determine their ability to reduce the stability and persistence of the insulating vapour film without external energy input. The objective was to assess whether these passive interventions can meaningfully shorten the high-risk film boiling window and thereby improve baseline system reliability. Figure 6(a) presents the cooling curves showing the individual and combined effects of the passive modifications applied to the system.

The introduction of a minimal concentration (0.001 mol/L) of TSP as an ionic additive yields a modest improvement in cooling performance. As shown in Fig. 6(a), the presence of TSP shifts the cooling curve leftward, raising the T_{min} from 281 °C (bare sample) to 298 °C. The observed enhancement is attributed to the chemical destabilization of the vapour-liquid interface. The dissociation of TSP produces phosphate anions (PO_4^{3-}), which, due to their relatively higher polarizability, exhibit enhanced affinity for the low-dielectric interface. In contrast, the smaller and strongly hydrated sodium cations (Na^+) preferentially remain solvated within the bulk liquid phase [53]. The preferential adsorption may impart a net negative charge to nascent bubbles, introducing a short-range electrostatic repulsion that can suppress early coalescence. The range of this force is defined by the Debye length (κ^{-1}):

$$\kappa^{-1} = \sqrt{\frac{\epsilon_r \epsilon_0 k_B T}{2 N_A e^2 I}} \tag{18}$$

Under current conditions, the theoretical κ^{-1} is 4 nm, indicating that any electrostatic barrier to bubble coalescence is confined to the near-interface region. While this mechanism facilitates earlier vapour rupture, the enhancement is marginal and consistent with studies employing low additive concentrations [41], indicating limited control under safety-critical conditions. Higher concentrations were avoided, as excessive ionic strength has been reported to stabilize the vapour–liquid interface, thereby prolonging film boiling and increasing thermal latency.

In contrast, the geometric modification induces a profound intensification of the transport process. Figure 6(a) demonstrates that the attachment of a 3-D cellular structure reduces the film boiling duration by 64%. Furthermore, the cellular surface achieves a T_{min} of 371 °C, representing a 90 °C elevation relative to the bare baseline. This significant performance gain is driven by geometric confinement, which physically disrupts the hydrodynamic stability of the vapour layer and reduces the persistence of the high-impedance state.

The stability of a vapour film on a plain surface is governed by the Rayleigh-Taylor instability, which dictates a critical wavelength $\lambda_H = 2\pi\sqrt{\frac{\sigma}{g(\rho_l - \rho_v)}}$ = 15.7 mm. The cellular structure features a characteristic cell dimension (D_{cell} = 1.3 mm) that is an order of magnitude smaller than this critical wavelength. Consequently, the geometric confinement prohibits the formation of a continuous stable vapour layer under transient quenching conditions.

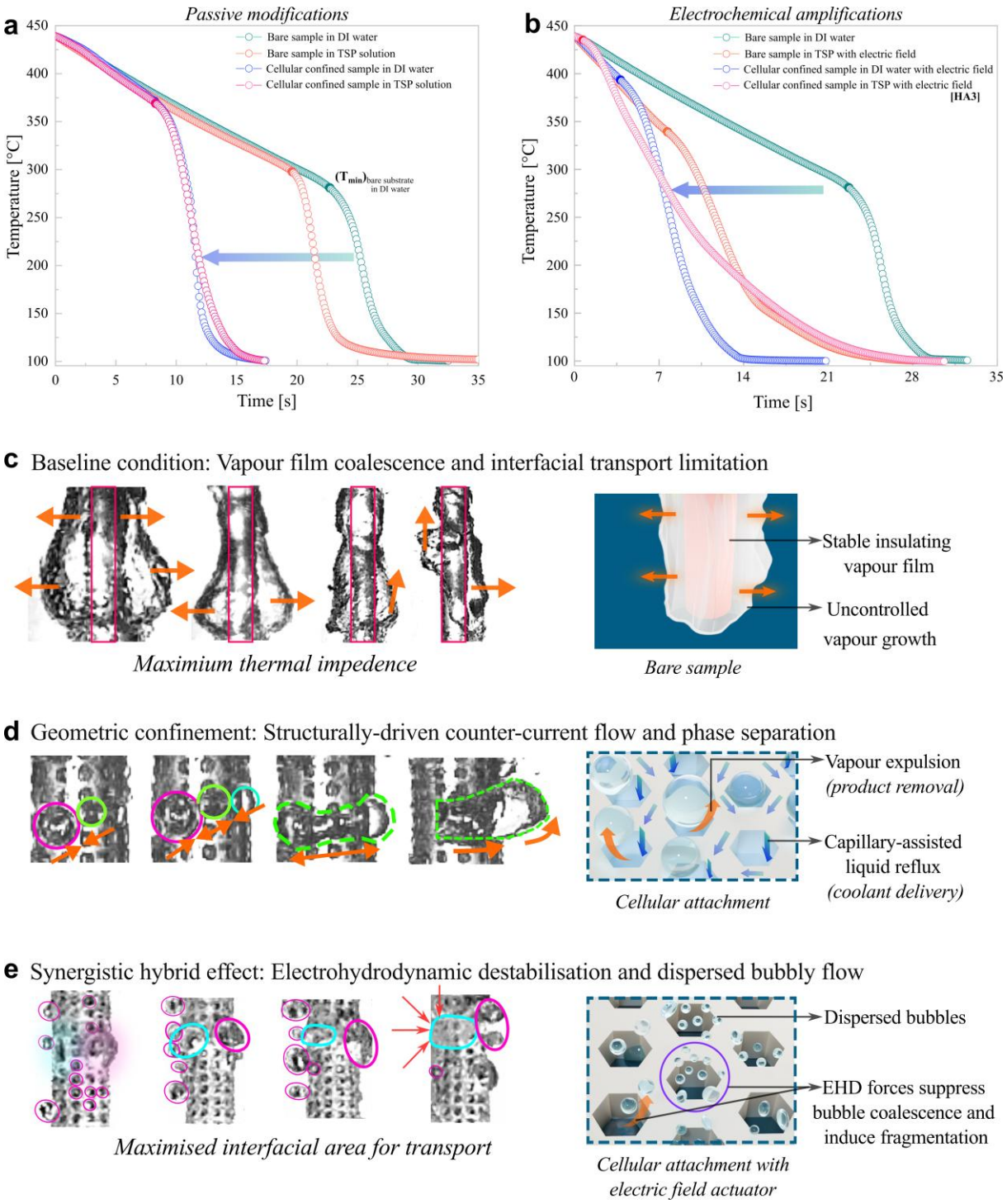


Figure 6. Performance characteristics and mechanistic validation. (a) Cooling profiles quantifying the thermal latency reduction via passive geometric and chemical modifications. (b) Operating envelope expansion under active electrohydrodynamic (EHD) actuation. (c-e) High-speed visualization and schematic illustration of the governing interfacial regimes: (c) baseline vapour film insulation; (d) architected phase separation via counter-current channelling; and (e) synergistic EHD-induced vapour fragmentation.

The open-cell structure and point-contact integration establish discrete, parallel pathways for counter-current liquid and vapour flow, promoting vigorous oscillation and early transition to the high-heat-flux nucleate boiling regime. High-speed visualization and corresponding schematic (Fig. 6 (c, d)) provide validation of this operational transition. As shown in Fig. 6(c), the baseline scenario is characterized by the immediate formation of a continuous, stable vapour film that acts as a macroscopic thermal impedance. The visualization confirms that this uncontrolled vapour growth physically isolates the solid surface, creating a stochastic barrier that chokes energy dissipation. In contrast, the cellular surface architecture (Fig. 6(d)) visually demonstrates the enforcement of deterministic phase separation. The cellular structure is observed to physically segregate the transport fluxes, maintaining open channels for vapour product removal (outward flow) while sustaining capillary-assisted coolant delivery (inward reflux). The architectural control effectively eliminates the chaotic coalescence observed in the baseline, converting the stochastic interference of the vapour film into structurally driven exchange regime that actively maintains thermodynamic accessibility. Crucially, the combination of geometric attachment and TSP additives yields a cooling profile almost identical to the geometry-only case. This observation confirms that the structurally dictated hydrodynamic effect is the dominant control parameter, rendering chemical modification insufficient as a standalone mitigation strategy for the transport limitations of film boiling.

3.3.2 Active intensification via electrohydrodynamic actuation

The application of an external electric field introduces a tuneable control actuator that enables deterministic regulation of interfacial transport, transforming the passive quenching configuration into an actively stabilized thermal management subsystem. As evidenced by the cooling profiles in Fig. 6(b), this active intervention significantly expands the safe operating envelope by reducing the persistence of vapour-induced thermal impedance during the high-superheat regime. For the bare sample in the 0.001 mol/L TSP solution, the application of a 200 V potential elevates T_{min} by 41 °C compared to the passive case, and by 58 °C relative to the baseline system. It shows that enhancement is driven by the dominance of electric field-induced transport over natural diffusion processes.

To get quantitative insights of this control mechanism, the transport dynamics of the working fluid were analysed. Under the applied potential of 200 V across an average vapour film thickness of 1 mm, the resulting electric field strength (2×10^5 V/m) imposes a directed electrohydrodynamic body force at the liquid–vapour interface. The calculated field-induced drift velocity, $v = \mu_{ion} E = 3.3 \times 10^{-2}$ m/s, is approximately four orders of magnitude greater

than the characteristic velocity of natural diffusion (5.3×10^{-6} m/s). Such disparity indicates that the system response is governed by field-driven interfacial forcing rather than slow, diffusion-limited transport processes. Consequently, the resulting Maxwell stress acts as a primary destabilizing force at the liquid-vapour interface, enabling the rupture of the insulating vapour film. This enhanced hydrodynamic instability intensifies interfacial mass transport by enforcing liquid-solid contact. Concurrently, the field-induced interfacial agitation provides a secondary mechanism for transport enhancement. The nucleation and departure of these bubbles create intense local micro-convection, disrupting the thermal boundary layer and augmenting heat removal through mechanical agitation.

However, the synergy between the electric field and the geometric surface modification yields the most profound performance gain. Figure 6(b) demonstrates that the combination of geometric attachment and the electric field increases the T_{min} by 112 °C compared to the baseline system, and by 22 °C compared to the passive geometric modification alone. This additional enhancement indicates that the electric field provides an active destabilization pathway that complements the hydrodynamic confinement. The open-cell configuration creates a heterogeneous field distribution, generating localized regions of high field intensity near the cell walls and edges. This non-uniformity induces steep pressure gradients at the liquid–vapour interface. At the cell walls, the amplified electric field imposes a local normal stress that destabilizes the vapour–liquid interface, while the open cell regions retain relatively higher vapour pressure. This imbalance alters the interfacial force balance, promoting the rapid instability of the liquid–vapour interface. The resultant destabilization facilitates an early and deterministic rupture of the vapour film, enhancing liquid rewetting and ensuring robust heat transfer performance at high superheats. The visualization shown in Fig. 6(e) confirms that the EHD actuator physically fragments the vapour phase, suppressing the formation of cohesive vapour masses and maintaining a maximized interfacial area for transport. This transition from geometric channelling to active fragmentation ensures that the surface remains continuously accessible to the liquid coolant. The intense, localized electrostatic pressure generates a normal stress gradient that overcomes the stabilizing forces of surface tension and vapour pressure, thereby suppressing vapour-induced thermal impedance and enabling reliable heat rejection under transient high-superheat conditions.

3.4 Accelerated energy dissipation under regulated thermal stress

The transient heat flux characteristics were analysed to evaluate the trade-off between cooling rate intensification and thermal-mechanical integrity of the component under safety-critical

quenching conditions. Figures 7(a) and 7(b) show the heat flux profiles for the passive and active configurations, respectively. A consistent leftward shift in the heat flux curves for the modified samples indicates an earlier onset of effective heat extraction.

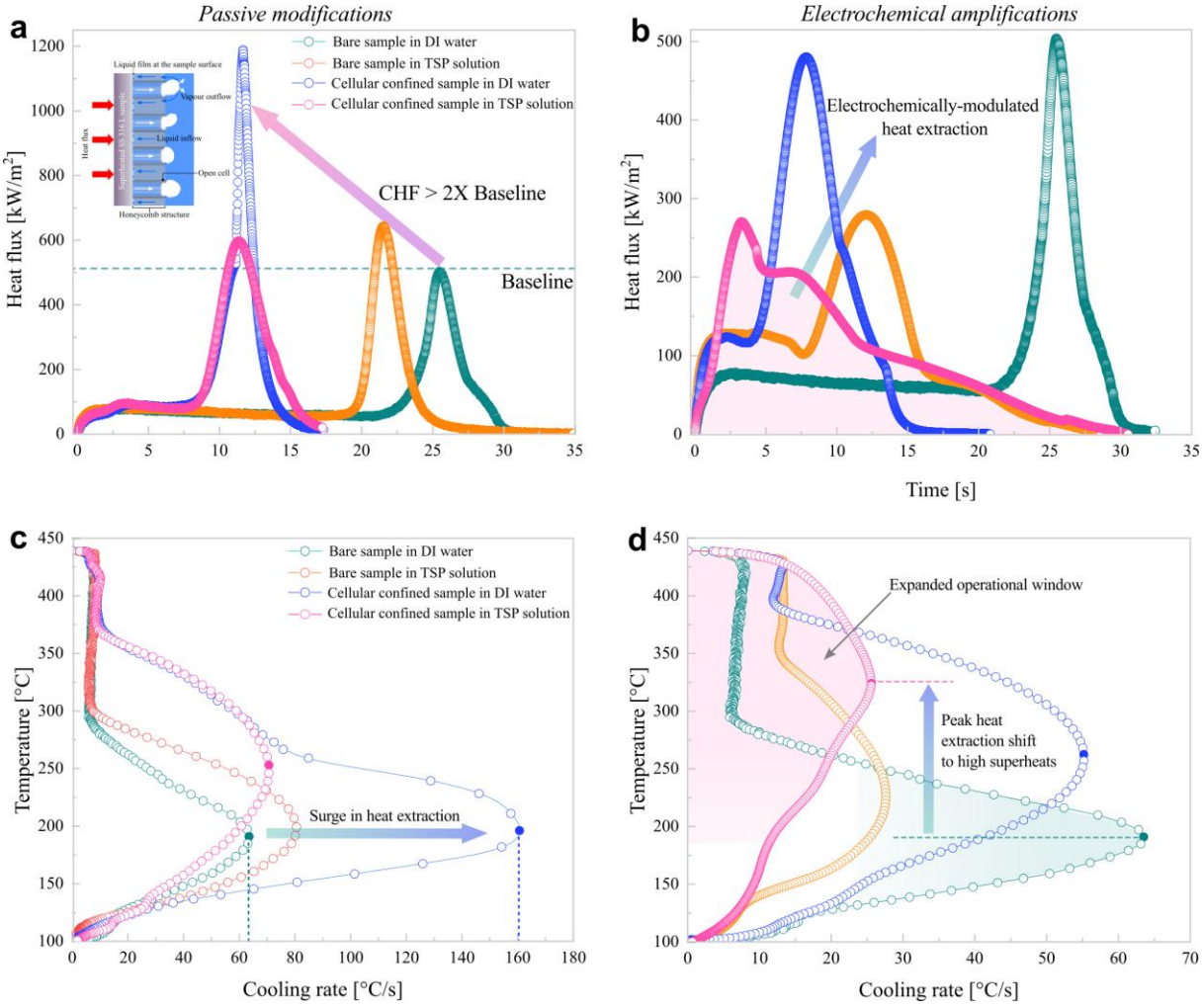


Figure 7. Heat flux characteristics under: (a) passive modifications; (b) active electrochemical modifications; and (c,d) cooling rate profiles confirming the regulation of transient thermal shock.

Figure 7(a) reveals that the passive geometric modifications drive the system toward a "thermal shock prone" regime. The sample with the cellular structure in DI water reaches a CHF of approximately 1190 kW/m² at 12 s, which is more than double that of the reference condition (500 kW/m² at 25 s). The insert in Fig. 7(a) shows enhanced liquid-vapour pathways at the cellular structure. While this increase confirms the strength of the hydrodynamic enhancement mechanism, the concentration of such a high heat load within a condensed timeframe introduces a thermal stress. The sudden rupture of the vapour film triggers a violent surge in bubble dynamics and a rapid escalation to peak heat flux. This sudden thermal impulse generates steep

temperature gradients and compressive stresses at the boiling surface, elevating the risk of thermal fatigue and reducing structural reliability over repeated operating cycles [54,55].

In contrast, the application of the electric field transforms the energy release profile from a damaging spike to a regulated discharge. As shown in Fig. 7(b), the active system significantly attenuates the peak thermal load. For the field-actuated sample with cellular attachment in DI water, the CHF is observed to be 480 kW/m² at 8 s. Similarly, in the TSP solution, the peak is modulated to 270 kW/m² at 3 s. This reflects pre-emptive redistribution of the stored thermal energy away from a single damaging peak. By destabilizing the vapour film immediately upon immersion, the active system dissipates a substantial portion of the stored thermal energy during the typically inefficient film and transition boiling regimes. Such early and continuous energy removal prevents the accumulation of the thermal load that drives the sharp CHF surge in the passive system. Consequently, the heat flux is distributed more evenly over the cooling duration, moderating the peak instantaneous rate and reducing the localized thermal gradients and stress concentration. The load-smoothing capability positions the hybrid approach as a reliability-oriented strategy for safety-critical thermal management, where protecting the component from transient thermal stress is prioritized over heat flux magnitude.

The analysis of cooling rate curves provides further insight into the system's ability to shape the transient energy release trajectory. Figure 7(c) reveals that under passive conditions, the cooling rate at high wall temperatures remains critically low, throttled by the dominant thermal resistance of the stable vapour film. This delay forces the system to reject the majority of its stored energy in a condensed, high-intensity surge at lower temperatures. For the reference sample, the peak cooling rate occurs at only 191 °C, indicating that the component remains in a high-risk thermal state for a prolonged duration before efficient heat transfer is engaged.

The introduction of the hybrid active control strategy fundamentally alters this profile, shifting the operational window of efficient cooling to higher temperatures. As evidenced in the cooling rate curves, the combination of coolant modification and surface attachment initiates an earlier transition to nucleate boiling. Consequently, the peak cooling rate shifts from 191 °C to 253 °C. The observed 62 °C elevation in the peak efficiency temperature signifies a meaningful expansion of the thermal safety margin, allowing the system to access high-performance cooling regimes earlier in the crisis timeline.

While the cellular structure in DI water achieves the highest instantaneous peak cooling rate, such surge represents a transient instability associated with the sudden establishment of liquid–

vapour contact. In contrast, the application of the electric field results in a distinct "peak broadening" effect, as shown in Fig. 7(d). This broadening indicates that stable transition and nucleate boiling are sustained over nearly the entire cooling duration, rather than being confined to a narrow, low-temperature spike. The electric field promotes this stability through two concurrent mechanisms: field-induced gas generation creates mechanical turbulence that disrupts the boundary layer, while the electrophoretic transport of the coolant ensures continuous liquid replenishment at the hot surface. Together, these active transport mechanisms overcome vapour-dominated thermal resistance, transforming the cooling process from a surge-dominated response into a sustained, rate-controlled operation that maintains high energy dissipation throughout the critical high-temperature window.

4. Conclusions

This work systematically addresses the process-design challenge of sustaining high and predictable energy extraction rates during vapour-dominated transient thermal operation. By coupling a conductive, point-contact surface architecture with electrohydrodynamic interfacial actuation, the proposed strategy re-establishes effective liquid-solid contact during the most critical early stages of quenching. The results demonstrate that vapour-mediated interfacial thermal resistance under transient conditions can be actively regulated through synergistic architectural enforcement and interface actuation. The key conclusions from this work are:

- The combined architectural and field-based intervention enables sustained coolant access to the heated surface during high-superheat operation, eliminating delayed rewetting behaviour that constrains passive systems. As a result, the cooling response transitions from an unregulated transient dominated by vapour persistence to a predictable, rate-controlled process.
- The analysis confirms a deliberate redistribution of irreversibility in time. Higher entropy generation is concentrated during the earliest phase of cooling, corresponding to restored thermal coupling and rapid energy extraction, while prolonged irreversibility associated with vapour persistence is averted. Such redistribution exhibits controllability of energy dissipation in transient processes.
- Neither geometric confinement nor electrohydrodynamic actuation alone is sufficient to sustain high-rate energy extraction under transient vapour-dominated conditions. Reliable process intensification is achieved only when architectural features define

deterministic flow pathways and active interfacial forcing facilitates vapour fragmentation to alleviate vapour accumulation.

- The hybrid configuration significantly increases energy extraction during the initial quenching window, when thermal resistance and operational risk are highest. By restoring effective transient thermal energy transport pathway at elevated temperatures, the system achieves a 2.7-fold increase in early-stage energy throughput.

In summary, this study establishes that the limitations imposed by vapour-mediated interfacial resistance during transient thermal operation can be addressed through coordinated architectural design and interface-targeted actuation. The results demonstrate that transient heat-transfer performance can be engineered through active regulation of interfacial dynamics rather than reliance on passive boiling behaviour alone. These findings provide experimentally grounded design guidance for thermal management systems in which energy extraction rate, operational stability, and auxiliary energy cost are simultaneously constrained.

Acknowledgement

The authors acknowledge the financial support received from Science and Engineering Research Board (SERB) under the scheme Core Research Grant (CRG) [Grant Award No.: CRG/2022/005638], Govt. of India, and the Department of Science and Technology, Govt. of India for supporting this work under the scheme FIST (No. SR/FST/ETI-388/2015). The work was also supported by the UK Engineering and Physical Sciences Research Council (EPSRC) [grant number EP/EP/T033398/1]. This work was also supported by a Marie Skłodowska-Curie Individual Fellowship under the European Union's Horizon 2020 Research and Innovation Programme (Grant Agreement No. 101028904) and European Union's Horizon Europe Research and Innovation Programme (Grant Agreement No. 101152661). Data supporting this publication can be obtained on request from cep-lab@imperial.ac.uk. For the purpose of Open Access, the authors have applied a CC BY public copyright licence to any Author Accepted Manuscript version arising from this submission.

References

[1] Papadis E, Tsatsaronis G. Challenges in the decarbonization of the energy sector. Energy 2020;205:118025. https://doi.org/https://doi.org/10.1016/j.energy.2020.118025.

[2] Oh J, Han U, Jung Y, Kang YT, Lee H. Advancing waste heat potential assessment for net-zero emissions: A review of demand-based thermal energy systems. Renew

Sustain Energy Rev 2024;202:114693. https://doi.org/https://doi.org/10.1016/j.rser.2024.114693.

[3] Gong T, Wu Y, Gao L, Zhang L, Li J, Ming T. Thermo-mechanical analysis on a compact thermoelectric cooler. Energy 2019;172:1211–24. https://doi.org/https://doi.org/10.1016/j.energy.2019.02.014.

[4] Li J, Tang A, Jin Y, Cai T, Dai S. Cooling performance enhancement and economic analysis of air conditioner systems integrated with phase change materials for telecommunication base station. Energy 2025;333:137297. https://doi.org/https://doi.org/10.1016/j.energy.2025.137297.

[5] Ni S, Pan C, Hibiki T, Zhao J. Applications of nucleate boiling in renewable energy and thermal management and recent advances in modeling——a review. Energy 2024;289:129962. https://doi.org/https://doi.org/10.1016/j.energy.2023.129962.

[6] Brooks D, Martonosi M. Dynamic thermal management for high-performance microprocessors. Proceedings HPCA Seventh International Symposium on High-Performance Computer Architecture, 2001, p. 171–82. https://doi.org/10.1109/HPCA.2001.903261.

[7] Coskun AK, Atienza D, Rosing TS, Brunschwiler T, Michel B. Energy-efficient variable-flow liquid cooling in 3D stacked architectures. 2010 Design, Automation & Test in Europe Conference & Exhibition (DATE 2010), 2010, p. 111–6. https://doi.org/10.1109/DATE.2010.5457228.

[8] Tsukamoto K, Kita Y, Inoue S, Hamanosono T, Hidaka S, Ueoka S, et al. On the onset of quench during spray cooling: The significance of oxide layers. Appl Therm Eng 2020;179:115682. https://doi.org/https://doi.org/10.1016/j.applthermaleng.2020.115682.

[9] Hadikhani P, Hashemi SMH, Schenk SA, Psaltis D. A membrane-less electrolyzer with porous walls for high throughput and pure hydrogen production. Sustain Energy Fuels 2021;5:2419–32. https://doi.org/10.1039/D1SE00255D.

[10] Fratalocchi L, Groppi G, Visconti CG, Lietti L, Tronconi E. Adoption of 3D printed highly conductive periodic open cellular structures as an effective solution to enhance the heat transfer performances of compact Fischer-Tropsch fixed-bed reactors. Chemical Engineering Journal 2020;386:123988. https://doi.org/https://doi.org/10.1016/j.cej.2019.123988.

[11] Inbaoli A, Krishnan A, Jehana V, Sujith Kumar CS, Gangolu S. Influence of alumina nanoparticle concentrations on quenching characteristics of cylindrical Al7075.

Thermal Science and Engineering Progress 2023;39:101687. https://doi.org/https://doi.org/10.1016/j.tsep.2023.101687.

[12] Xu N, Yu X, Liu Z, Zhang T, Chu H. Effects of chloride ion concentration on porous surfaces and boiling heat transfer performance of porous surfaces. Energy 2024;294. https://doi.org/10.1016/j.energy.2024.130818.

[13] Cho J, Doan TL, Lee S, Kim IG, Jang S, Shao Y, et al. Porous transport electrodes for oxygen evolution reaction in proton exchange membrane water electrolysis -cells: Materials, designs, and diagnoses. Chemical Engineering Journal 2025;507:160473. https://doi.org/https://doi.org/10.1016/j.cej.2025.160473.

[14] Kou T, Wang S, Shi R, Zhang T, Chiovoloni S, Lu JQ, et al. Periodic Porous 3D Electrodes Mitigate Gas Bubble Traffic during Alkaline Water Electrolysis at High Current Densities. Adv Energy Mater 2020;10:2002955. https://doi.org/https://doi.org/10.1002/aenm.202002955.

[15] Hu Y, Xu Z, Shi H, Wang B, Wang L, Zhang L-W. Understanding ultrafast free-rising bubble capturing on nano/micro-structured super-aerophilic surfaces. Nat Commun 2025;16:3682. https://doi.org/10.1038/s41467-025-59049-x.

[16] Liu B, Liu X, Tang S, Li Q, Zhang Y. Micro-nano composited surfaces for boiling front propagation restriction and pool boiling performance enhancement. Appl Therm Eng 2025;280:128437. https://doi.org/https://doi.org/10.1016/j.applthermaleng.2025.128437.

[17] Zhao J, Yang X, Zhu D. Three-dimensional biphilic structures elevating pool boiling heat transfer. Energy 2025;320:135353. https://doi.org/https://doi.org/10.1016/j.energy.2025.135353.

[18] Inbaoli A, Sujith Kumar CS, Jayaraj S. A review on techniques to alter the bubble dynamics in pool boiling. Appl Therm Eng 2022;214:118805. https://doi.org/10.1016/j.applthermaleng.2022.118805.

[19] Liang G, Mudawar I. Pool boiling critical heat flux (CHF) – Part 1: Review of mechanisms, models, and correlations. Int J Heat Mass Transf 2018;117:1352–67. https://doi.org/10.1016/j.ijheatmasstransfer.2017.09.134.

[20] Wang J, He Y, Song Z. Enhanced flow boiling heat transfer performance of diamond microchannels: An experimental study. Energy 2025;333. https://doi.org/10.1016/j.energy.2025.137316.

[21] Qiu S, Wang S, Nour M, Li X, Xu M, Wang L, et al. Experimental study on flow fields of spray impingement under flash boiling conditions. Energy 2025;318:134748. https://doi.org/https://doi.org/10.1016/j.energy.2025.134748.

[22] Ahangar Zonouzi S, Aminfar H, Mohammadpourfard M. A review on effects of magnetic fields and electric fields on boiling heat transfer and CHF. Appl Therm Eng 2019;151:11–25. https://doi.org/10.1016/j.applthermaleng.2019.01.099.

[23] Li B, Wang X, Li N, Tam L, Zeng M, Wang Q. Thermal management of integrated circuits in energy systems: Flow boiling in microchannels with multiple ultra-high heat flux sources. Energy 2025;322. https://doi.org/10.1016/j.energy.2025.135533.

[24] Sudha A, Santoso A, Rohde M. Influence of a 'Step' on the liquid–liquid flow patterns and flow phenomena in a microfluidic Y-Y channel. Chemical Engineering Journal 2025;512:161823. https://doi.org/https://doi.org/10.1016/j.cej.2025.161823.

[25] Du H, Liang X, Yang W, Vujanović M, Wang J, He Y. Effect of surface modification with copper nanowire arrays on nucleate boiling in a liquid cooler. Energy 2025;335. https://doi.org/10.1016/j.energy.2025.138168.

[26] Lai K, Yang S, Wang H. Numerical investigation of bubble dynamics and multi-scale flow characteristics in the bottom-blown gas–liquid reactor. Chemical Engineering Journal 2023;474:145868. https://doi.org/https://doi.org/10.1016/j.cej.2023.145868.

[27] Matsushima H, Iida T, Fukunaka Y. Gas bubble evolution on transparent electrode during water electrolysis in a magnetic field. Electrochim Acta 2013;100:261–4. https://doi.org/https://doi.org/10.1016/j.electacta.2012.05.082.

[28] Lao L, Ramshaw C, Yeung H. Process intensification: water electrolysis in a centrifugal acceleration field. J Appl Electrochem 2011;41:645–56. https://doi.org/10.1007/s10800-011-0275-2.

[29] Celestini F, Kirstetter G. Effect of an electric field on a Leidenfrost droplet. Soft Matter 2012;8:5992–5. https://doi.org/10.1039/C2SM25656H.

[30] Quinn A, Sedev R, Ralston J. Contact Angle Saturation in Electrowetting. J Phys Chem B 2005;109:6268–75. https://doi.org/10.1021/jp040478f.

[31] Saccone G, Garivalis AI, Di Marco P. Electrohydrodynamics and boiling: Experiments, numerical calculation and modeling of Maxwell stress tensor and electric force acting on bubbles. J Electrostat 2020;103:103413. https://doi.org/https://doi.org/10.1016/j.elstat.2019.103413.

[32] Wei X, Kakimoto T, Umehara Y, Nakajima H, Ito K, Inagaki H, et al. Improvement of the critical current density of alkaline water electrolysis based on the hydrodynamic

similarity between boiling and water electrolysis. Int J Heat Mass Transf 2023;214:124420. https://doi.org/https://doi.org/10.1016/j.ijheatmasstransfer.2023.124420.

[33] Shahriari A, Hermes M, Bahadur V. Electrical control and enhancement of boiling heat transfer during quenching. Appl Phys Lett 2016;108:091607. https://doi.org/10.1063/1.4943230.

[34] Inbaoli A, Krishnan A, Jehana V, Sujith Kumar CS, Gangolu S. Influence of alumina nanoparticle concentrations on quenching characteristics of cylindrical Al7075. Therm Sci Eng Prog 2023;39:101687. https://doi.org/10.1016/j.tsep.2023.101687.

[35] Inbaoli A, Sujith Kumar CS, Jayaraj S. Experimental investigation on the effect of additives on different orientations of Al6061 cylindrical sample during immersion quenching. Appl Therm Eng 2022;204:118030. https://doi.org/https://doi.org/10.1016/j.applthermaleng.2021.118030.

[36] Inbaoli A, Sujith Kumar CS, Chougule SS, Markides CN, S J. Enhanced electrolytic immersion cooling for thermal crisis mitigation in high-energy–density systems. Energy Convers Manag 2024;300:117980. https://doi.org/10.1016/j.enconman.2023.117980.

[37] Elhadad AA, Rosa-Sainz A, Cañete R, Peralta E, Begines B, Balbuena M, et al. Applications and multidisciplinary perspective on 3D printing techniques: Recent developments and future trends. Materials Science and Engineering: R: Reports 2023;156:100760. https://doi.org/https://doi.org/10.1016/j.mser.2023.100760.

[38] Hsu SH, Ho YH, Ho MX, Wang JC, Pan C. On the formation of vapor film during quenching in de-ionized water and elimination of film boiling during quenching in natural sea water. Int J Heat Mass Transf 2015;86:65–71. https://doi.org/10.1016/j.ijheatmasstransfer.2015.02.049.

[39] Babu K, Prasanna Kumar TS. Effect of CNT concentration and agitation on surface heat flux during quenching in CNT nanofluids. Int J Heat Mass Transf 2011;54:106–17. https://doi.org/https://doi.org/10.1016/j.ijheatmasstransfer.2010.10.003.

[40] Venkitesh V, Dash S. Enhancement of quenching heat transfer performance through destabilization of vapor film. Int J Heat Mass Transf 2023;204:123851. https://doi.org/https://doi.org/10.1016/j.ijheatmasstransfer.2023.123851.

[41] Kumar V, Sinha KNR, Raj R. Leidenfrost phenomenon during quenching in aqueous solutions: effect of evaporation-induced concentration gradients. Soft Matter 2020;16:6145–54. https://doi.org/10.1039/D0SM00622J.

[42] Babu K, Prasanna Kumar TS. Mathematical Modeling of Surface Heat Flux During Quenching. Metallurgical and Materials Transactions B 2010;41:214–24. https://doi.org/10.1007/s11663-009-9319-y.

[43] Kumar TS. A SERIAL SOLUTION FOR THE 2-D INVERSE HEAT CONDUCTION PROBLEM FOR ESTIMATING MULTIPLE HEAT FLUX COMPONENTS. Numerical Heat Transfer, Part B: Fundamentals 2004;45:541–63. https://doi.org/10.1080/10407790490277940.

[44] Arunkumar S, Sreenivas Rao K V, Prasanna Kumar TS. Spatial variation of heat flux at the metal–mold interface due to mold filling effects in gravity die-casting. Int J Heat Mass Transf 2008;51:2676–85. https://doi.org/https://doi.org/10.1016/j.ijheatmasstransfer.2007.10.020.

[45] Kumar TP. Coupled analysis of surface heat flux, microstructure evolution, and hardness during immersion quenching of a medium carbon steel in plant conditions. Mater Perform Charact 2012;1:MPC104477.

[46] Lee SG, Kaviany M, Lee J. Role of quenching method on cooling rate and microstructure of steels: Variations in coolant and its flow arrangement. Int J Heat Mass Transf 2022;189:122702. https://doi.org/https://doi.org/10.1016/j.ijheatmasstransfer.2022.122702.

[47] Cheng H-C, Lin H-C, Chen P-H. Boiling heat transfer enhancement over copper tube via electrolytic and electrostatic effects. Appl Therm Eng 2021;199:117584. https://doi.org/https://doi.org/10.1016/j.applthermaleng.2021.117584.

[48] Blackwell B, Beck J V. A technique for uncertainty analysis for inverse heat conduction problems. Int J Heat Mass Transf 2010;53:753–9. https://doi.org/https://doi.org/10.1016/j.ijheatmasstransfer.2009.10.014.

[49] Fan LW, Li JQ, Zhang L, Yu ZT, Cen KF. Pool boiling heat transfer on a nanoscale roughness-enhanced superhydrophilic surface for accelerated quenching in water. Appl Therm Eng 2016;109:630–9. https://doi.org/10.1016/j.applthermaleng.2016.08.131.

[50] Zhang JY, Li JQ, Jiang LY, Fan LW, Yu ZT. Pool boiling heat transfer during quenching on a superhydrophilic surface in dilute aqueous saline solutions: Effects of the solution concentration and type of salts. Int J Heat Mass Transf 2019;138:1117–27. https://doi.org/10.1016/j.ijheatmasstransfer.2019.04.127.

[51] Niblett D, Elwan HA, Mamlouk M. Membraneless water electrolysis enabled by flow and porous electrode design for bubble separation. Chemical Engineering Journal 2025;519:163444. https://doi.org/https://doi.org/10.1016/j.cej.2025.163444.

[52] Li Z, Cai P, Yang J, Shao M, Xu J, Wang H. Mechanistic impact of Stern bilayer-based electrolysis on the enhancement of pool boiling heat transfer. Therm Sci Eng Prog 2024;55:102908. https://doi.org/https://doi.org/10.1016/j.tsep.2024.102908.

[53] Son CY, Wang Z-G. Image-charge effects on ion adsorption near aqueous interfaces. Proceedings of the National Academy of Sciences 2021;118:e2020615118. https://doi.org/10.1073/pnas.2020615118.

[54] Motallebi R, Savaedi Z, Mirzadeh H. Additive manufacturing – A review of hot deformation behavior and constitutive modeling of flow stress. Curr Opin Solid State Mater Sci 2022;26:100992. https://doi.org/https://doi.org/10.1016/j.cossms.2022.100992.

[55] Morales NG, Fleck TJ, Rhoads JF. The effect of interlayer cooling on the mechanical properties of components printed via fused deposition. Addit Manuf 2018;24:243–8. https://doi.org/https://doi.org/10.1016/j.addma.2018.09.001.